remote sensing

MDPI

Article

Pulse RFI Mitigation for SAR Data Based on Reduced Rank Approximate

Bingxu Chen [1], Weiwei Fan [1,*], Siyu Chen [1], Zongsen Lv [2] and Feng Zhou [3]

[1] The Key Laboratory of Electronic Information Countermeasure and Simulation Technology, Ministry of Education, Xidian University, Xi'an 710071, China; chenbingxu@stu.xidian.edu.cn (B.C.)
[2] The Shanghai Institute of Satellite Engineering, Shanghai 201109, China
[3] The School of Aerospace Science and Technology, Xidian University, Xi'an 710071, China
* Correspondence: wwfan@xidian.edu.cn

Highlights

What are the main findings?

- A novel semi-parametric PRFI mitigation method is proposed, in which the Hankel structure inherits and enhances PRFI's low-rank property, while truncated nuclear norm (TNN) regularization is introduced to replace the traditional nuclear norm, providing a more precise rank approximation and avoiding the over-penalization of all singular values.
- The proposed method achieved the best RMSE in the simulation experiments under different parameter settings. In two measured experiments on Sentinel-1A, the proposed method improves average gradient (AG) by **16.03%** and **18.67%** over the best competing method, and reduces multiplicative noise ratio (MNR) by **3.06 dB** and **1.26 dB** over the best competitor.

What are the implications of the main findings?

- The method mitigates strong wideband PRFI without the signal loss of notch filtering or the singular-value over-penalization of nuclear-norm methods, preserving fine ground-feature details in SAR imagery.
- It offers a transferable low-rank framework for wideband PRFI mitigation, extendable to other SAR systems and RFI types.

Abstract

Radio frequency interference (RFI) caused by spectrum allocation issues can adversely affect the normal operation of synthetic aperture radar (SAR). Compared to traditional RFI, pulsed RFI (PRFI) typically has higher power and wider bandwidth, making the resulting artifacts more likely to obscure the targets of interest. The notch filtering methods are robust approaches to mitigating PRFI. However, the proportion of PRFI in SAR data increases as the electromagnetic environment gradually deteriorates, and these methods inevitably lose too much useful signal. Moreover, traditional semi-parametric methods based on nuclear norms (NNs) over-penalize singular values, leading to the inaccurate estimation of low-rank components. To overcome the aforementioned problems, this article proposes a semi-parametric method. Our method is based on the Hankel structure and truncated nuclear norm (TNN) constrained low-rank estimation model to mitigate strong PRFI while preserving valuable signals. First, the SAR echoes containing PRFI are detected using a relative energy ratio algorithm. Then, the low-rank properties of PRFI are linearly expanded and enhanced through the Hankel structure. Finally, TNN regularization is employed to obtain more accurate low-rank approximations than traditional NN, thereby separating

Check for updates

Academic Editor: Fabio Rocca

Received: 30 May 2026
Revised: 23 July 2026
Accepted: 23 July 2026
Published: 1 August 2026

Copyright: © 2026 by the authors. Licensee MDPI, Basel, Switzerland. This article is an open access article distributed under the terms and conditions of the Creative Commons Attribution (CC BY) license.

PRFI. Experiments based on simulated and measured data from ESA Sentinel-1A validated the usefulness and preeminence of our method.

Keywords: synthetic aperture radar (SAR); pulsed radio frequency interference (PRFI); Hankel structure; low-rank estimation model; truncated nuclear norm (TNN)

1. Introduction

1.1. Background

Synthetic aperture radar (SAR) emits electromagnetic waves in the range direction that can penetrate clouds, rain, fog, and achieve high-resolution ground observation through pulse compression technology [1]. In the azimuth direction, it achieves high-resolution target observations through synthetic aperture techniques [2]. Compared to optical remote sensing sensors, SAR systems can operate normally 24 h a day under adverse weather conditions, making them indispensable in the remote sensing field [3]. Moreover, as the application fields and mission requirements diversify, SAR systems have developed multiple operating modes and are exploring more advanced new systems [4,5].

Modern radio technology has entered a period of prosperous development, with a surge of various radio services emerging, including but not limited to navigation systems, positioning services, communication systems, television, and cellular networks [6]. Although these radio services have greatly improved people's lives, they have made the limited spectrum increasingly crowded, thereby exacerbating the problem of SAR systems suffering from same-frequency radio frequency interference (RFI) pollution caused by these services [7]. Figure 1 illustrates the main RFI events detected by Sentinel-1A during its 242nd orbital cycle. The common version of RFI, namely pulse RFI (PRFI), is tricky in SAR systems. It can produce periodic bright stripes and rain/fog-like artifacts in SAR images and affect subsequent SAR data applications [8]. PRFI is a direct wave signal, and compared to traditional RFI, it possesses higher power and wider bandwidth [9]. Therefore, researching mitigation algorithms for PRFI is more challenging.

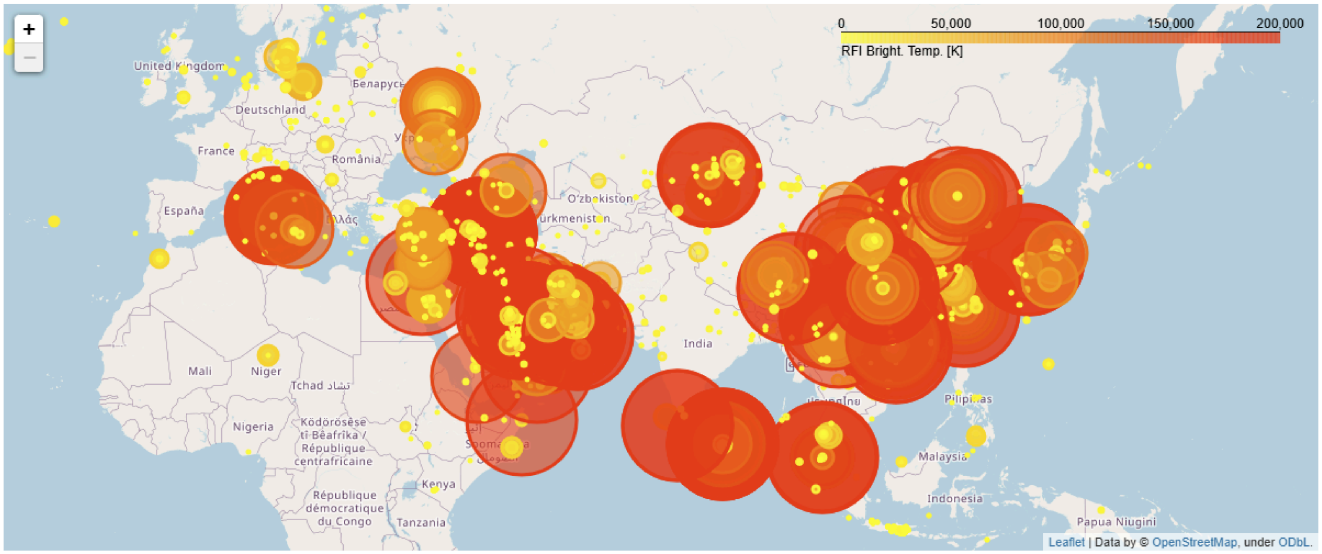


Figure 1. The main RFI events detected by the ESA Sentinel-1A during its 242nd orbital cycle.

1.2. Research Progress of RFI Mitigation

Over the past thirty-plus years, many experts and scholars have proposed a series of methods to mitigate RFI [10].

(1) *Parametric Methods:* These methods model RFI as a superposition of a series of FM signals and then accurately reconstruct and remove the RFI components by estimating the model parameters. These methods require high precision in parameter estimation; when the parameter estimation is inaccurate, the interference mitigation performance can be significantly degraded. For narrowband interference (NBI) mitigation, maximum likelihood estimation [11], least mean square estimation [12], and least squares estimation [13] have been used to estimate NBI parameters. These classical methods are effective for relatively simple and stationary NBI, but their performance is sensitive to model mismatch, initialization, and the accuracy of frequency and amplitude estimation. Moreover, they are generally less suitable for nonstationary or wideband interference (WBI) with time-varying modulation. The iterative adaptive approach provides high-resolution spectral estimation and has been applied to NBI and WBI mitigation [14,15], but it requires iterative computation and accurate estimation of the interference spectrum. Regularized time–frequency (TF) filtering can handle nonstationary WBI by estimating its instantaneous frequency trajectory [16], although its performance depends on TF resolution and estimation accuracy. Dechirping converts LFM-type WBI into NBI for efficient mitigation [17], but it is sensitive to chirp-rate errors and model mismatch. Recently, Nie et al. proposed an off-grid RFI mitigation method based on mismatch reconstruction and dictionary rotation [18], which improves frequency-matching accuracy but requires iterative dictionary optimization. Qiu et al. developed a TJLS matrix-decomposition method to automatically extract weak-RFI parameters in the TF domain [19]; however, its accuracy depends on the TF resolution and matrix decomposition performance. Mao et al. proposed a group-parametric model that refines both the RFI and target models [20], achieving improved interference mitigation and scene preservation at the cost of increased model and computational complexity.

(2) *Semi-parametric Methods:* These methods do not need excessively precise parameter estimation; instead, they use hyperparameter optimization to solve the SAR echo signals iteratively [21]. Nguyen et al. pioneered RFI mitigation research based on sparse recovery by decomposing NBI-contaminated SAR data into sparse and low-rank components, where the former represents the useful SAR signal and the low-rank component corresponds to NBI [22]. Subsequently, the same team investigated an improved method that joins down-range and cross-range to suppress interference [23]. Su et al. utilized the TF low-rank property of NBI to eliminate interference [24]. Huang et al. introduced a series of optimization models that jointly low-rank and sparse to rapidly mitigate both NBI and WBI [25–28]. Lu et al. developed a regularization model in the image domain to mitigate interference [29]. Su et al. proposed a TF-pulse joint decomposition approach to mitigate WBI [30]. It is essential to note that semi-parametric approaches involve extensive iterative processing and matrix inversion operations, which significantly increase the computational complexity of these approaches.

(3) *Non-parametric Methods:* These methods utilize the different feature intensities between SAR signals and RFI in the transform domain to achieve interference mitigation. Due to their lack of reliance on prior knowledge and precise models of RFI, these methods are widely applied. Notch filtering and its variants transform the RFI-containing SAR signals into a domain with prominent interference features, and then set the interference components to zero to mitigate RFI [9,31]. Nevertheless,

when mitigating WBI with long pulse widths, the effectiveness of the aforementioned approaches significantly decreases. Matrix decomposition methods are also classical non-parametric approaches. Based on the orthogonality of RFI in the subspace, Zhou et al. projected interference onto a subspace to mitigate NBI [32]. In addition, the team proposed a series of decomposition methods to mitigate strong RFI [33–35]. Most of these methods operate in the raw-echo domain; therefore, some image-domain methods have been proposed, such as subband spectral cancellation [36], image-domain sparse regularization [37], Lambda-1 detector [38], and block subspace filtering [39,40]. Chen et al. proposed an automatic processing flow for RFI detection and mitigation applicable to the LuTan-1 to handle a large number of interfered images [41]. These methods can be applied to single-look complex image products to mitigate specific types of RFI.

1.3. Problem Statement

Easy-to-implement and robust notch filtering methods can be employed to address the PRFI problem. The frequency-domain notch filtering (FNF) method aggregates PRFI's energy in the frequency domain through range Fourier transform and then applies notch processing. However, PRFI typically has higher power and wider bandwidth because it primarily originates from ground-based radar systems such as meteorological radar, early warning radar, and marine radar. This means that the FNF method will create unexpected spectral gaps, leading to anomalous point target responses. The time-domain notch filtering (TNF) method is not affected by the PRFI bandwidth [42]. Nevertheless, it requires accurate acquisition of PRFI location information; otherwise, its mitigation performance will be severely limited. Moreover, as the proportion of PRFI in SAR echoes increases, the TNF method will notch filter out more useful signals, inevitably creating echo gaps that lead to azimuthal ghosting, thereby affecting the interpretation of SAR images.

Semi-parametric methods can also be employed to address the problem of RFI. Most semi-parametric approaches, such as robust principal component analysis (RPCA) [22] and go decomposition (GoDec) [43], rely on the RFI constraint of the nuclear norm (NN). Nevertheless, the NN simultaneously minimizes all singular values of the matrix, which means that such low-rank estimations are susceptible to errors. The direct consequence of this issue is the tendency to excessively penalize singular values, thereby diminishing the performance of RFI mitigation. RPCA and GoDec typically perform low-rank–sparse decomposition directly in the original echo domain. The former adopts the conventional NN, whereas the latter relies on fixed-rank approximation. Although weighted nuclear norm methods can mitigate, to some extent, the excessive shrinkage of singular values caused by the conventional NN, they still improve rank approximation mainly from the perspective of singular-value weighting and do not explicitly model the time-delay structure of PRFI. Time–frequency low-rank decomposition methods, by contrast, rely on the energy-concentration characteristics in the time–frequency transform domain, and their performance may be affected by the time–frequency representation and parameter selection.

1.4. Proposed Method and Contributions

Inspired by the aforementioned issues, a novel semi-parametric method is proposed. Our method is based on the Hankel structure and truncated nuclear norm (TNN) regularized low-rank approximation model to mitigate strong PRFI and preserve valuable SAR signals simultaneously. In the proposed method, a Hankel matrix of PRFI-contaminated SAR echo can be constructed using the time delay embedding (TDE) theory, where the low-rank property of the PRFI with overwhelming power can be linearly extended to the

Hankel matrix. Subsequently, a low-rank approximation model regularized by a TNN is established. Unlike the traditional NN, the TNN only minimizes the smallest portion of the singular values. This provides stronger rank approximation capabilities, thereby enabling more accurate recovery of low-rank components. Finally, a two-stage iterative method is proposed to unravel the TNN-regularized optimization issue, thereby effectively extracting and separating the PRFI components.

The main contributions:

(1) The article proposes a novel semi-parametric approach. The approach is based on the Hankel structure and a TNN-regularized low-rank approximation model. This approach effectively mitigates strong PRFI while preserving valuable signals. The Hankel structure is capable of both linearly inheriting and enhancing PRFI's low-rank property, resulting in more concentrated PRFI characteristics.
(2) Compared to most semi-parametric methods that utilize the NN, the proposed method employs TNN, which offers a more precise approximation of the rank operator. Consequently, it achieves a more precise recovery of low-rank components. Additionally, unlike notch filtering methods, the approach does not require the acquisition of PRFI location information and avoids the significant loss of valuable signals.
(3) Abundant experiments were conducted based on simulated interference data to evaluate the PRFI mitigation performance under various PRFI parameters. Additionally, experiments using Sentinel-1A Level-0 measured data were performed to validate the proposed approach's effectiveness and excellence.

1.5. Thesis Structure

The subsequent structure is as follows. Section 2 discusses the modeling of PRFI, along with the formulation of the related problem. Section 3 details the proposed semi-parametric approach. Our approach is based on a Hankel structure and a TNN-regularized low-rank approximation model. Section 4 provides abundant experimental results, qualitative and quantitative evaluations, and a thorough outcomes analysis. A detailed discussion is provided in Section 5. Finally, Section 6 pithily summarizes the paper.

2. Models and Characteristics of Pulse Radio Frequency Interference

2.1. Spatiotemporal Model

This kind of interference typically arises from direct wave signals generated by ground-based radio equipment such as wind profilers, telecommunication wireless communication posts, ground-based radio positioning radars, etc. Beyond terrestrial sources, there is a growing body of reports on direct wave mutual PRFI occurring between satellites [44,45]. In practice, the occurrence of PRFI impact on the SAR system generally requires the following conditions: (1) overlapping working time, i.e., the working time of the PRFI source fully or partially coincides with that of the SAR system; (2) overlapping working frequency, i.e., the frequency band utilized by the PRFI source overlaps with that of the SAR system; and (3) overlapping working spatial, i.e., the signals transmitted by the PRFI source must be receivable by the SAR receiver.

Figure 2 illustrates the spatial relationships between the potential PRFI sources and the SAR system, along with a signal timing diagram. From Figure 2a, it is evident that PRFI transmitted by the interference source follows a single-direction propagation path and is received by the SAR. In Figure 2b, the timing indicates that the SAR system is contaminated by interference only when the intrusion time of PRFI coincides with the SAR receiver's working time.

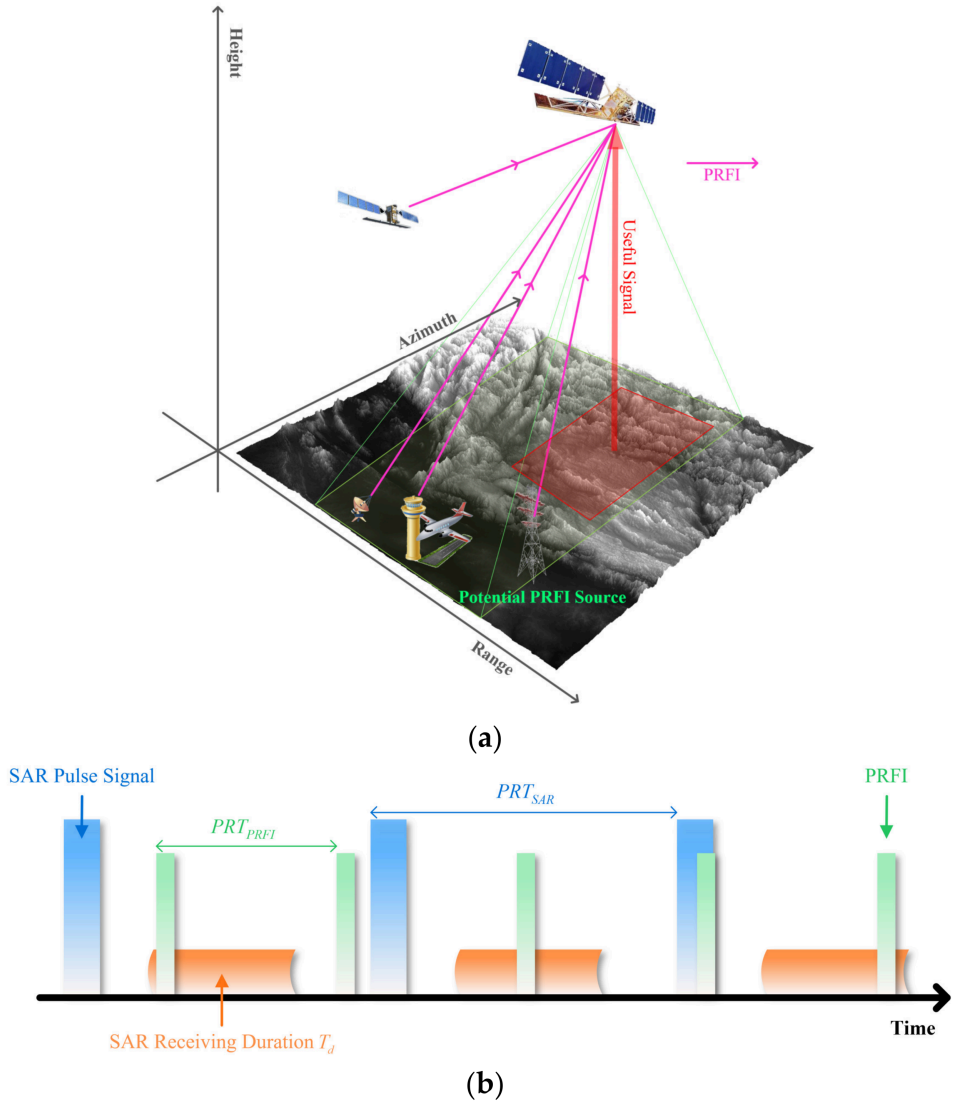


Figure 2. Spatiotemporal model between PRFI sources and SAR system. (**a**) Spatial relationship. (**b**) The signal timing diagram.

2.2. Signal Model

The data received by systems is typically defined as a 2D discrete-time matrix [46]. After being processed by the SAR receiver, the SAR signal contaminated by PRFI is modeled as

$$R(\tau,\eta) = S(\tau,\eta) + N(\tau,\eta) + I(\tau,\eta) \tag{1}$$

where $S(\tau,\eta)$ is a SAR signal, $I(\tau,\eta)$ as a interference signal, $N(\tau,\eta)$ represents a noise signal, τ denotes the range time, and η is the azimuth time.

The mathematical formula of interference is represented as

$$\begin{aligned} I(\tau,\eta) = \sum_{n=1}^{N} A_n \mathrm{rect}\left(\frac{\tau}{T_d}\right)\mathrm{rect}\left(\frac{\tau-\tau_d(\eta)}{T_n}\right) \\ \times \exp(j(2\pi f_n(\tau-\tau_d(\eta)) + \varphi_n(\tau-\tau_d(\eta)))) \end{aligned} \tag{2}$$

where A_n denotes the amplitude of the nth interference; f_n denotes the PRFI frequency; T_d represents the SAR receiving duration; τ_d is the delay of the interference; N is the number of interference; $\varphi_n(\cdot)$ denotes the modulation phase. The type of PRFI is determined by

$\varphi_n(\cdot)$. When $\varphi_n(\cdot) = 0$, the PRFI is narrowband PRFI (NPRFI). The modulation type of wideband PRFI (WPRFI) is typically modeled as linear FM or sinusoidal FM:

$$I_{LFM}(\tau,\eta) = \sum_{n=1}^{N} A_n \mathrm{rect}\left(\frac{\tau}{T_d}\right)\mathrm{rect}\left(\frac{\tau-\tau_d(\eta)}{T_n}\right) \times \exp(2j\pi f_n(\tau-\tau_d(\eta))) \times \exp\left(j\pi K_n(\tau-\tau_d(\eta))^2\right) \tag{3}$$

$$I_{SFM}(\tau,\eta) = \sum_{n=1}^{N} A_n \mathrm{rect}\left(\frac{\tau}{T_d}\right)\mathrm{rect}\left(\frac{\tau-\tau_d(\eta)}{T_n}\right) \times \exp(j\beta_n \sin(2\pi f_n(\tau-\tau_d(\eta)))) \tag{4}$$

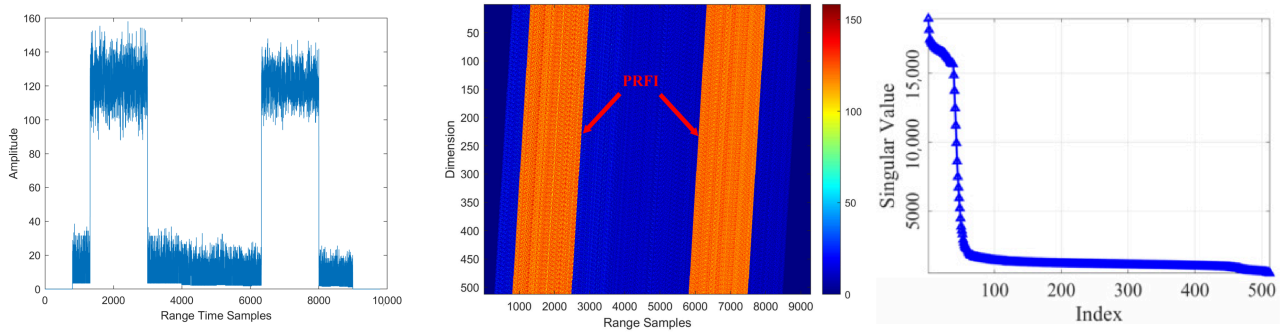
where K_n is the range frequency modulation of the nth interference component, and β_n denotes the modulation factor.

3. PRFI Mitigation via Hankel Structure and Truncated Nuclear Norm Regularization

3.1. Problem Formulation

This paper observes that the Hankel structure of PRFI can enhance its low-rank property. In other words, the SAR pulses contaminated by PRFI can be restructured into a Hankel structure through time-delay embedding (TDE) theory, thereby linearly inheriting and amplifying the low-rank attribute of high-power PRFI within the Hankel matrix. Enhancing PRFI's low-rank property can improve the accuracy of PRFI component extraction in the LRSD model, thereby minimizing the loss of valuable signals and enhancing the algorithm's mitigation performance.

To demonstrate how the Hankel structure enhances PRFI's low-rank property, PRFI-contaminated SAR echoes acquired from ESA's Sentinel-1A are used, with results shown in Figure 3. In Figure 3a, a measured SAR echo is contaminated by PRFI, where two abrupt transitions represent two instances of PRFI. Figure 3b displays the Hankel structure derived from the SAR echo in Figure 3a. It is observed that the PRFI's low-rank property is linearly inherited and amplified within the Hankel matrix. Figure 3c presents the singular values of the Hankel-structured SAR pulses. The fewer prominent singular values and steeper singular-value decay indicate that the Hankel-structured SAR echo has a lower rank, demonstrating that its low-rank property is significantly enhanced.



(**a**) (**b**) (**c**)

Figure 3. Diagram of low-rankness of PRFI-contaminated SAR echo. (**a**) The measured SAR pulse. (**b**) The Hankel-structured SAR pulse. (**c**) The singular values of the Hankel-structured SAR pulse.

Based on the aforementioned findings, a PRFI-contained SAR echo is constructed in a Hankel structure. Specifically, (1) can be represented in discrete form as follows:

$$\boldsymbol{R} = \boldsymbol{S} + \boldsymbol{N} + \boldsymbol{I} \tag{5}$$

where

$$\begin{aligned}\boldsymbol{R} &= \begin{bmatrix} R(1) & R(2) & \dots & R(N_r) \end{bmatrix} \in \mathbb{C}^{N_r} \\ \boldsymbol{S} &= \begin{bmatrix} S(1) & S(2) & \dots & S(N_r) \end{bmatrix} \in \mathbb{C}^{N_r} \\ \boldsymbol{N} &= \begin{bmatrix} N(1) & N(2) & \dots & N(N_r) \end{bmatrix} \in \mathbb{C}^{N_r} \\ \mathbf{I} &= \begin{bmatrix} I(1) & I(2) & \dots & I(N_r) \end{bmatrix} \in \mathbb{C}^{N_r}\end{aligned} \tag{6}$$

and N_r represents the number of sampling points in the fast time dimension.

Subsequently, all measured values in (5) are organized into a Hankel matrix:

$$\begin{aligned}\mathbf{R} &= \boldsymbol{\mathcal{H}}(\boldsymbol{R}) \\ &= \boldsymbol{\mathcal{H}}(\boldsymbol{S}) + \boldsymbol{\mathcal{H}}(\boldsymbol{N}) + \boldsymbol{\mathcal{H}}(\boldsymbol{I}) \\ &= \boldsymbol{S} + \boldsymbol{N} + \boldsymbol{I}\end{aligned} \tag{7}$$

where $\boldsymbol{\mathcal{H}}(\cdot)$ denotes the operation of constructing the Hankel matrix.

Taking the Hankel matrix $\mathbf{R}$ as an example, it can be expressed as follows:

$$\begin{aligned}\boldsymbol{R} &= \boldsymbol{\mathcal{H}}(\boldsymbol{R}) \\ &= \begin{bmatrix} \boldsymbol{R}(1) & \boldsymbol{R}(2) & \dots & \boldsymbol{R}(M) \\ \boldsymbol{R}(2) & \boldsymbol{R}(3) & \dots & \boldsymbol{R}(M+1) \\ \vdots & \vdots & \ddots & \vdots \\ \boldsymbol{R}(L) & \boldsymbol{R}(L+1) & \dots & \boldsymbol{R}(M+L-1) \end{bmatrix} \in \mathbb{C}^{L \times M}\end{aligned} \tag{8}$$

where L denotes the number of rows in $\mathbf{R}$ and $M = N_r - L + 1$. The Hankel structures corresponding to the other three measurements in (7) are the same as those shown in (8).

Figure 4 illustrates the LRSD of a Hankel-structured pulse. Similar to the semi-parametric approach for sparse SAR signal and low-rank RFI, PRFI can be separated by leveraging the Hankel structure of the low-rank matrix. Inspired by the traditional low-rank representation (LRR) model, ℓ_0 regularization is employed to preserve the sparse SAR signal, and the problem can be modeled as follows:

$$\begin{aligned}\min_{\mathbf{I},\mathbf{S}} \ & rank(\mathbf{I}) + \lambda \|\mathbf{S}\|_0 \\ s.t. \ & \mathbf{R} = \mathbf{I} + \mathbf{S}\end{aligned} \tag{9}$$

where $rank(\cdot)$ is the rank function, $\|\cdot\|_0$ denotes the ℓ_0 norm (i.e., the number of nonzero elements in the matrix), and λ is the regularization parameter.

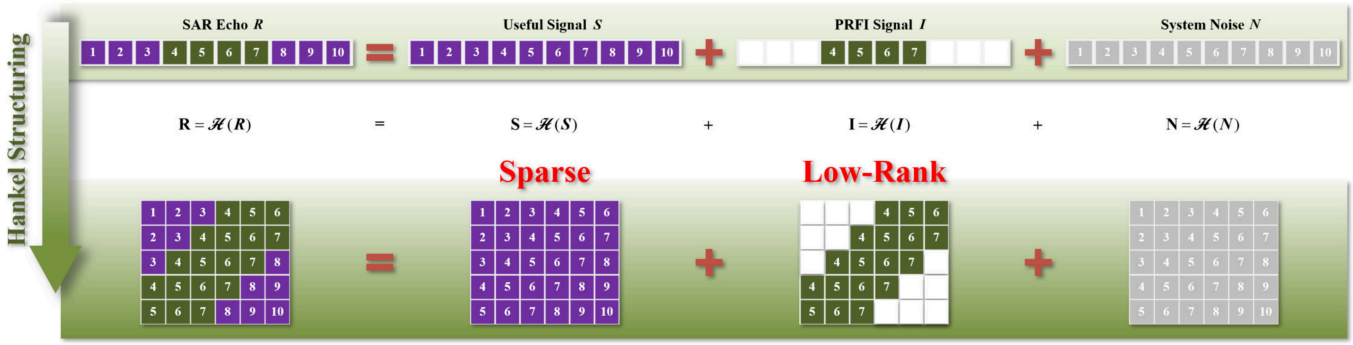


Figure 4. Illustration of the low rankness of the Hankel-structured SAR pulse.

Note that because the rank function is non-convex and discrete, and so is the ℓ_0 norm, problem (9) is non-deterministic polynomial hard. Most existing LRSD algorithmcand ℓ_1 norm to resolve the ℓ_0 norm. Therefore, problem (9) can be reformulated as follows:

$$\begin{aligned} \min_{\mathbf{I},\mathbf{S}} \ & \|\mathbf{I}\|_* + \lambda\|\mathbf{S}\|_1 \\ s.t. \ & \mathbf{R} = \mathbf{I} + \mathbf{S} \end{aligned} \tag{10}$$

where $\|\cdot\|_*$ is the NN, i.e., the summation of the singular values for a matrix, whereas $\|\cdot\|_1$ is the ℓ_1 norm, i.e., the summation of absolute values for a matrix.

3.2. Model Improvement via TNN Regularization

In the NN, each nonzero singular value of the matrix contributes differently. However, the rank minimization in problem (10) usually tends to penalize large singular values excessively. This issue prevents the NN from accurately approximating the rank operator, which may lead to inaccurate recovery of the low-rank components using NN-based LRSD methods, ultimately affecting the interference mitigation performance. Inspired by this issue, TNN is introduced here as a better alternative to the traditional NN. By optimizing only the total of a few smallest singular values—since larger singular values contribute less to rank minimization—TNN can provide a more precise approximation. Consequently, problem (10) is updated as

$$\begin{aligned} \min_{\mathbf{I},\mathbf{S}} \ & \|\mathbf{I}\|_{r,*} + \lambda\|\mathbf{S}\|_1 \\ s.t. \ & \mathbf{R} = \mathbf{I} + \mathbf{S} \end{aligned} \tag{11}$$

where $\|\cdot\|_{r,*}$ is TNN, i.e., the summation of the smallest singular values.

However, since TNN is a non-convex rank function, the proposed model (11) is NP-hard and cannot be solved directly. To address this problem, let $\mathbf{I} = \mathbf{U}\sum\mathbf{V}^T$ denote the SVD of matrix $\mathbf{I}$, truncating $\mathbf{U} = (\mathbf{u}_1, \ldots, \mathbf{u}_m) \in \mathbb{C}^{m\times m}$ and $\mathbf{V} = (\mathbf{v}_1, \ldots, \mathbf{v}_n) \in \mathbb{C}^{n\times n}$ into $\mathbf{A}$ and $\mathbf{B}$, that is

$$\begin{aligned} \mathbf{A} &= (\mathbf{u}_1, \ldots, \mathbf{u}_r)^T \\ \mathbf{B} &= (\mathbf{v}_1, \ldots, \mathbf{v}_r)^T \end{aligned} \tag{12}$$

where r signifies the quantity of truncated singular values, and $(\cdot)^T$ specifies transposition. Then, the TNN term can be recast by using Theorem 3.1 in [47]

$$\begin{aligned} \|\mathbf{I}\|_{r,*} &= \sum_{i=r+1}^{\min(m,n)} \sigma_i(\mathbf{I}) = \sum_{i=1}^{\min(m,n)} \sigma_i(\mathbf{I}) - \sum_{i=1}^{r} \sigma_i(\mathbf{I}) \\ &= \|\mathbf{I}\|_* - \max_{\mathbf{A}\mathbf{A}^T=\mathbf{E},\mathbf{B}\mathbf{B}^T=\mathbf{E}} \left\{ \mathrm{Tr}\left(\mathbf{A}\mathbf{I}\mathbf{B}^T\right) \right\} \end{aligned} \tag{13}$$

where E denotes an $r \times r$ identity matrix, while $\sigma(\cdot)$ represents a singular value, and $Tr(\cdot)$ signifies the trace.

Accordingly, the problem (11) can be relaxed as

$$\begin{aligned} \min_{\mathbf{I},\mathbf{S}} & \|\mathbf{I}\|_* - \max_{\mathbf{A}\mathbf{A}^T=\mathbf{E},\mathbf{B}\mathbf{B}^T=\mathbf{E}} \left\{ \mathrm{Tr}\left(\mathbf{A}\mathbf{I}\mathbf{B}^T\right) \right\} + \lambda\|\mathbf{S}\|_1 \\ s.t. \ & \mathbf{R} = \mathbf{I} + \mathbf{S} \end{aligned} \tag{14}$$

3.3. Solution for (14) Based on the Two-Stage Iterative Algorithm

To solve (14), an effective solution is proposed using a two-stage iterative process. At the beginning, $\mathbf{A}$ and $\mathbf{B}$ are computed from the fixed $\mathbf{R}$ using SVD, while the second stage updates $\mathbf{I}$ and $\mathbf{S}$ with fixed $\mathbf{A}$ and $\mathbf{B}$. The algorithm alternates between these two stages

until convergence. In the second stage, the following optimization problem is solved to update $\mathbf{I}$ and $\mathbf{S}$:

$$\begin{aligned} \min_{\mathbf{I},\mathbf{S}} &\|\mathbf{I}\|_* - \mathrm{Tr}\left(\mathbf{A}_l\mathbf{I}\mathbf{B}_l^T\right) + \lambda\|\mathbf{S}\|_1 \\ &s.t.\ \mathbf{R} = \mathbf{I} + \mathbf{S} \end{aligned} \tag{15}$$

In this paper, we utilize the ADMM framework to address (15) in an alternating manner. First, the augmented Lagrangian function of (15) is

$$\begin{aligned} \mathcal{L}(\mathbf{I},\mathbf{S},\mathbf{Y},\mu) = &\|\mathbf{I}\|_* - \mathrm{Tr}\left(\mathbf{A}_l\mathbf{I}\mathbf{B}_l^T\right) + \lambda\|\mathbf{S}\|_1 \\ &+\langle\mathbf{Y},\mathbf{R}-\mathbf{I}-\mathbf{S}\rangle + \tfrac{\mu}{2}\|\mathbf{R}-\mathrm{I}-\mathbf{S}\|_F^2 \end{aligned} \tag{16}$$

where $\mathbf{Y}$ and $\mu > 0$ denote the Lagrange multiplier and penalty parameter, respectively; $\langle\cdot,\cdot\rangle$ and $\|\cdot\|_F$ represent the inner product and Frobenius norm, respectively. Subsequently, problem (15) can be solved by alternately updating one variable while keeping the others fixed according to the ADMM framework. Specifically, for the kth iteration, the subproblems to be solved are

$$\begin{cases} \mathbf{I}_{k+1} = \mathrm{argmin}_{\mathbf{I}}\mathcal{L}(\mathbf{I},\mathbf{S}_k,\mathbf{Y}_k,\mu_k) \\ \mathbf{S}_{k+1} = \mathrm{argmin}_{\mathbf{S}}\mathcal{L}(\mathbf{I}_{k+1},\mathbf{S},\mathbf{Y}_k,\mu_k) \\ \mathbf{Y}_{k+1} = \mathbf{Y}_k + \mu_k(\mathbf{R}-\mathbf{I}_{k+1}-\mathbf{S}_{k+1}) \\ \mu_{k+1} = \min(\rho\mu_k,\mu_{\max}) \end{cases} \tag{17}$$

where $\rho > 1$. In this solution, $\mathbf{I}$ and $\mathbf{S}$ are updated through the resolution of subproblems (17), which have closed-form solutions. The details are explained below.

Update $\mathbf{I}_{k+1}$: For the update of $\mathbf{I}$, first fix $\mathbf{S}$, $\mathbf{Y}$ and μ. Accordingly, $\mathbf{I}$ can be updated by solving the following subproblem:

$$\begin{aligned} \mathbf{I}_{k+1} &= \mathrm{argmin}_{\mathbf{I}}\|\mathbf{I}\|_* - \mathrm{Tr}\left(\mathbf{A}_l\mathbf{I}\mathbf{B}_l^T\right) \\ &\quad +\langle\mathbf{Y}_k,\mathbf{R}-\mathbf{I}-\mathbf{S}_k\rangle + \frac{\mu_k}{2}\|\mathbf{R}-\mathbf{I}-\mathbf{S}_k\|_F^2 \\ &= \mathrm{argmin}_{\mathbf{I}}\|\mathbf{I}\|_* + \frac{\mu_k}{2}\left\|\mathbf{I} - \left(\mathbf{R}-\mathbf{S}_k + \frac{\mathbf{A}_l^T\mathbf{B}_l+\mathbf{Y}_k}{\mu_k}\right)\right\|_F^2 \end{aligned} \tag{18}$$

Here, subproblem (18) can be effectively solved using the singular value shrinkage operator [48], and the solution can be expressed as

$$\mathbf{I}_{k+1} = \mathrm{SVS}_{\frac{1}{2\mu_k}}\left[\frac{1}{2}\left(\mathbf{R}-\mathbf{S}_k + \frac{\mathbf{A}_l^T\mathbf{B}_l+\mathbf{Y}_k}{\mu_k}\right)\right] \tag{19}$$

where $\mathrm{SVS}_{\frac{1}{2\mu_k}}(\cdot)$ is the singular value shrinkage operator.

Update S_{k+1}: Similarly, by fixing $\mathbf{I}$, $\mathbf{Y}$ and μ, the subproblem can be solved, allowing $\mathbf{S}$ to be updated

$$\begin{aligned} \mathbf{S}_{k+1} &= \mathrm{argmin}_{\mathbf{S}}\lambda\|\mathbf{S}\|_1 + \langle\mathbf{Y}_k,\mathbf{R}-\mathbf{I}_{k+1}-\mathbf{S}\rangle \\ &\quad +\tfrac{\mu_k}{2}\|\mathbf{R}-\mathbf{I}_{k+1}-\mathbf{S}\|_F^2 \\ &= \mathrm{argmin}_{\mathbf{S}}\lambda\|\mathbf{S}\|_1 + \tfrac{\mu_k}{2}\left\|\mathbf{S} - \left(\mathbf{R}-\mathbf{I}_{k+1}+\tfrac{\mathbf{Y}_k}{\mu_k}\right)\right\|_F^2 \end{aligned} \tag{20}$$

The aforementioned subproblem is capable of being efficiently addressed using the soft-thresholding operator:

$$\mathbf{S}_{k+1} = \mathrm{sgn}\left(\mathbf{R}-\mathbf{I}_{k+1}+\frac{\mathbf{Y}_k}{\mu_k}\right)\left(\left|\mathbf{R}-\mathbf{I}_{k+1}+\frac{\mathbf{Y}_k}{\mu_k}\right| - \frac{\lambda}{\mu_k}\right) \tag{21}$$

The updates for $\mathbf{Y}$ and μ can be accomplished through the last two lines of (17).

3.4. PRFI Mitigation via Hankel Structure and TNN

The proposed method based on the Hankel structure and TNN regularized low-rank approximation model should only handle SAR echoes contaminated by PRFI. Therefore, the relative energy ratio algorithm is proposed to detect SAR echoes affected by PRFI:

$$\delta_i = \frac{\max[\mathrm{FT}(\boldsymbol{R}_i)]}{E[\mathrm{FT}(\boldsymbol{R}_i)]} \tag{22}$$

where i represents the ith pulse, $\max(\cdot)$ indicates the extraction of the maximum value, $E(\cdot)$ denotes mean calculation, $\mathrm{FT}(\cdot)$ signifies FFT, and $i \le N_a$. The threshold ψ is set: if $\delta_i \ge \psi$, then the echo $\boldsymbol{R}_i$ is considered to contain PRFI; if $\delta_i < \psi$, then the echo $\boldsymbol{R}_i$ is not contaminated by PRFI:

$$\begin{cases} \delta_i \ge \psi \Rightarrow \boldsymbol{R}_i \quad with \;\; PRFI \\ \delta_i < \psi \Rightarrow \boldsymbol{R}_i \quad without \;\; PRFI \end{cases} \tag{23}$$

The threshold ψ is generally set between 2 and 10. Interference detection is performed on a pulse-by-pulse basis.

Execute the proposed algorithm process on SAR echoes contaminated by PRFI, and upon reaching the algorithm convergence criterion, obtain the Hankel structure PRFI component $\mathbf{I}$, and the sparse component $\mathbf{S}$, which is the Hankel structure signal matrix. Algorithm 1 summarizes the processing flow for ease of understanding. It should be noted that signal reconstruction needs to be performed on $\mathbf{S}$ to obtain SAR echoes without PRFI, that is:

Algorithm 1. PRFI Mitigation via Hankel Structure and TNNR

Input: $\boldsymbol{R}$, r, λ, μ_0, ρ, ε, ε_0, ψ, N_a;
Initialize: $i = 1, l = 1, k = 1, \mathbf{I}_1 = \mathbf{S}_1 = \mathbf{Y}_1 = 0$.

Repeat
  $\delta_i = \max[\mathrm{FT}(\boldsymbol{R}_i)] / E[\mathrm{FT}(\boldsymbol{R}_i)]$;
  If $\delta_i \ge \psi$
    $\mathbf{R}_i = \mathcal{H}(\mathbf{R}_i)$; Given $\mathbf{R}_l = \boldsymbol{R}_i$;
    Repeat
      Stage 1.
        $[\mathbf{U}_l, \sum_l, \mathbf{V}_l] = \mathrm{SVD}(\mathbf{R}_l)$;
        truncate $\mathbf{U}_l$ and $\mathbf{V}_l$ into $\mathbf{A}_l = (\mathbf{u}_1, \ldots, \mathbf{u}_r)^T$ and $\mathbf{B}_l = (\mathbf{v}_1, \ldots, \mathbf{v}_r)^T$;
      Stage 2.
        Repeat
          $\mathbf{I}_{k+1} = \mathrm{SVS}_{1/2\mu_k}\left[\left(\mathbf{R} - \mathbf{S}_k + \left(\mathbf{A}_l^T \mathbf{B}_l + \mathbf{Y}_k\right)/\mu_k\right)/2\right]$;
          $\mathbf{S}_{k+1} = \mathrm{ST}_{\lambda/\mu_k}(\mathbf{R} - \mathbf{I}_{k+1} + \mathbf{Y}_k/\mu_k)$;
          $\mathbf{Y}_{k+1} = \mathbf{Y}_k + \mu_k(\mathbf{R} - \mathbf{I}_{k+1} - \mathbf{S}_{k+1})$;
          $\mu_{k+1} = \min(\rho\mu_k, \mu_{\max})$;
        Until $\|\mathbf{I}_{k+1} - \mathbf{I}_k\|_F \le \varepsilon$ or $\|\mathbf{S}_{k+1} - \mathbf{S}_k\|_F \le \varepsilon$;
      $\mathbf{R}_{l+1} = \mathbf{I}_{k+1} + \mathbf{S}_{k+1}$;
    Until $\|\mathbf{R}_{l+1} - \mathbf{R}_l\|_F \le \varepsilon_0$
  End
  $i = i + 1, l = 1, k = 1, \mathbf{I}_1 = \mathbf{S}_1 = \mathbf{Y}_1 = 0$;
Until $i > N_a$
Output: PRFI matrix $\mathbf{I}$ and signal matrix $\mathbf{S}$.

$$S = \left[\mathbf{S}(1,:), (\mathbf{S}(M+1:M+L-1,M))^T\right] \in \mathbb{C}^{1\times N_r} \tag{24}$$

Perform the above processing on PRFI-contaminated SAR pulses in a pulse-by-pulse manner to obtain clean SAR data.

3.5. Computational Complexity

Let N_a and N_r denote the numbers of azimuth pulses and range samples, respectively, and let N_p denote the number of PRFI-contaminated pulses detected by the relative energy ratio method. The detection stage requires range FFTs and has a complexity of $\mathcal{O}(N_a N_r log N_r)$. For each contaminated pulse, an $L \times M$ Hankel matrix is constructed, where $M = N_r - L + 1$. The dominant operation in Stage 1 is the SVD, whose complexity is $\mathcal{O}\left(min\left(LM^2, L^2M\right)\right)$. In each ADMM iteration of Stage 2, the update of the low-rank component involves singular-value shrinkage and therefore requires another SVD, whereas the updates of the sparse component, Lagrange multiplier, and residuals require only $\mathcal{O}(LM)$ elementwise operations. Let K_o and K_i denote the numbers of outer TNN iterations and inner ADMM iterations, respectively. The overall computational complexity is therefore

$$\mathcal{O}\left(N_a N_r log N_r + N_p K_o (K_i + 1) LM min(L, M)\right) \tag{25}$$

When $L \leq M$, it can be written as

$$\mathcal{O}\left[N_a N_r log N_r + N_p K_o (K_i + 1) L^2 (N_r - L + 1)\right] \tag{26}$$

Although the proposed method is computationally more expensive than non-iterative notch-filtering methods because of the repeated SVD operations, only the detected PRFI-contaminated pulses are processed. Therefore, the practical computational cost is reduced when $N_p \ll N_a$.

3.6. Convergence Analysis

The proposed two-stage algorithm contains an outer TNN iteration and an inner ADMM iteration. At the l-th outer iteration, $\mathbf{R}_l$, $\mathbf{A}_l$, and $\mathbf{B}_l$ are kept fixed during the inner ADMM iterations. Accordingly, problem (15) can be written as

$$\begin{gathered} \min_{\mathbf{I},\mathrm{S}} \|\mathbf{I}\|_* - \mathrm{Tr}\left(\mathbf{A}_l \mathbf{I} \mathbf{B}_l^T\right) + \lambda \|\mathbf{S}\|_1 \\ s.t.\ \mathbf{R}_l = \mathbf{I} + \mathbf{S} \end{gathered} \tag{27}$$

The nuclear norm $\|\cdot\|_*$ and the ℓ_1 norm are closed convex functions, the trace term is linear with respect to $\mathbf{I}$, and the equality constraint is affine. Therefore, for fixed $\mathbf{R}_l$, $\mathbf{A}_l$, and $\mathbf{B}_l$, problem (15) is convex. Under the standard assumption that an optimal solution exists and each variable subproblem is solved exactly, the corresponding two-block ADMM iterations converge to an optimal solution of problem (15).

To monitor the convergence of the inner ADMM iterations, the normalized primal residual is defined as

$$e_{\mathrm{p}}^{(k)} = \frac{\left\|\mathbf{R}_l - \mathbf{I}^{(k)} - \mathbf{S}^{(k)}\right\|_F}{\|\mathbf{R}_l\|_F} \tag{28}$$

The normalized dual residual is defined as

$$e_{\mathrm{d}}^{(k)} = \frac{\mu_k \left\|\mathbf{S}^{(k)} - \mathbf{S}^{(k-1)}\right\|_F}{\|\mathbf{R}_l\|_F} \tag{29}$$

Under the standard ADMM convergence conditions

$$\begin{cases} e_{\mathrm{p}}^{(k)} \to 0 \\ e_{\mathrm{d}}^{(k)} \to 0 \end{cases} \tag{30}$$

The penalty parameter is updated according to

$$\mu_{k+1} = \min(\rho\mu_k, \mu_{\max}), \qquad \rho > 1 \tag{31}$$

Since $\mu_k \leq \mu_{\max}$, it reaches $\mu_{\max}$ after a finite number of updates and subsequently remains constant. Therefore, the continuation strategy affects mainly the early convergence speed, whereas the inner iterations asymptotically reduce to standard ADMM with the fixed penalty parameter $\mu_{\max}$.

For the outer iteration, the TNN can be written as

$$\|\mathbf{R}\|_{r,*} = \|\mathbf{R}\|_* - \|\mathbf{R}\|_{(r)} \tag{32}$$

where

$$\|\mathbf{R}\|_{(r)} = \sum_{i=1}^{r} \sigma_i(\mathbf{R}) \tag{33}$$

According to the variational representation in (13), the matrices $\mathbf{A}_l$ and $\mathbf{B}_l$, obtained from the SVD of $\mathbf{R}_l$, construct a tight convex approximation of the original TNN objective at the current outer iterate. If each inner problem is solved exactly or with sufficient accuracy, the original TNN regularization objective values satisfy the following:

$$\Phi_{l+1} \leq \Phi_l \tag{34}$$

Moreover,

$$\|\mathbf{R}\|_{r,*} = \sum_{i=r+1}^{\min(L,M)} \sigma_i(\mathbf{R}) \geq 0 \tag{35}$$

and $\lambda\|\mathbf{S}\|_1 \geq 0$. Hence, the objective-value sequence is non-increasing and lower bounded, and therefore convergent. Under the above assumptions, every accumulation point satisfies the stationarity conditions of the original TNN-regularized problem. Since the TNN formulation is nonconvex, convergence to a global optimum cannot generally be guaranteed.

The inner ADMM iterations are terminated when

$$\begin{cases} e_{\mathrm{p}}^{(k)} < \varepsilon \\ e_{\mathrm{d}}^{(k)} < \varepsilon \end{cases} \tag{36}$$

or when the maximum number of inner iterations is reached. The outer iteration is terminated when

$$\frac{\|\mathbf{R}_{l+1} - \mathbf{R}_l\|_F}{\max(\|\mathbf{R}_l\|_F, 10^{-12})} < \varepsilon_0 \tag{37}$$

or when the maximum number of outer iterations is reached.

4. Numerical Experiment

To verify the proposed approach's performance, this part presents and analyzes the results. First, simulated experiments with various PRFI parameters are conducted to evaluate our approach's performance, and the root mean square error (RMSE) serves as a quantitative tool for analyzing results. Measured experimental results from ESA Sentinel-1A further validate the proposed approach's effectiveness, using three representative

methods as comparisons: FNF, TNF, PRCA and the Greedy Bilateral Smoothing LRSD algorithm (GBSLRSD) [49]. The results are quantitatively evaluated using the multiplicative noise ratio (MNR) and average gradient (AG). Additionally, this section provides detailed information on simulation parameters, measured SAR data, and quantitative metrics.

4.1. Evaluation Metrics

In the simulation experiments, the RMSE is used as the metric for quantitative analysis. RMSE indicates the difference between interference-free data and data after interference mitigation. A smaller RMSE signifies better performance in mitigation. $\mathbf{P}$ denotes the interference-free data, and $\widetilde{\mathbf{P}}$ signifies the data after mitigation. RMSE is calculated using the following formula

$$\mathrm{RMSE}\left(\mathbf{P},\widetilde{\mathbf{P}}\right)=\frac{\left\|\mathbf{P}-\widetilde{\mathbf{P}}\right\|_F}{\|\mathbf{P}\|_F} \tag{38}$$

In the measured experiments, MNR and AG are used as quantitative indicators to evaluate mitigation performance. MNR is used to assess the interference-mitigated SAR image, representing the degree of interference mitigation. A smaller MNR indicates more effective interference mitigation. The mathematical expression for MNR is

$$MNR=10\log_{10}\frac{\sum_{n=1}^{N_1}\left|D_n^{(1)}\right|^2/N_1}{\sum_{n=1}^{N_2}\left|D_n^{(2)}\right|^2/N_2} \tag{39}$$

where $D_n^{(1)}$ represents the pixel intensity in the weak-echo region, $D_n^{(2)}$ indicates the pixel intensity in the strong echo area, and N_1 and N_2 indicate the number of pixels. The "weak-echo region" refers to regions in the image with low backscattering intensity, relatively homogeneous texture, and no obvious strong scattering points or complex ground-object structures, such as sea surfaces, water bodies, dark background areas, or homogeneous low-scattering surfaces. This type of region is more sensitive to residual PRFI signatures, noise elevation, and artifacts, and is therefore suitable for evaluating the residual noise level after interference mitigation. The "strong-echo region" refers to regions in the image with stable and relatively strong backscattering, such as urban buildings, harbor facilities, or other structural ground objects. This region is used to represent the reference intensity of the useful SAR scene signal, thereby normalizing the residual interference in the weak-echo region.

AG denotes the average rate of gray-level change, reflecting the characteristics of detail and texture variations in the image as well as the image's clarity. AG is expressed as

$$AG=\frac{\sum_{i=1}^{M}\sum_{j=1}^{N}\sqrt{\left((\partial G/\partial x)^2+(\partial G/\partial y)^2\right)/2}}{M*N} \tag{40}$$

where G represents the image, M and N indicate the side lengths of G, and $\partial G/\partial y$ and $\partial G/\partial x$ represent the vertical and horizontal gradient values of G, respectively. Generally, a larger AG signifies a clearer image.

4.2. Simulated Experimental Results

The simulation scenario is based on the ESA Sentinel-1A strip mode observation of the Port of Santos in Brazil. The simulation parameters and the parameters of different PRFIs are displayed in Table 1. In the simulation experiment, the ratio of PRFI bandwidth to SAR bandwidth, known as the interference-to-signal bandwidth ratio (ISBR), is **60%**,

and the PRFI pulse width is set at **10–25 μs**, with a step of 5 μs. The signal-to-interference ratio (SIR) is **−30 dB**.

Table 1. Parameters of simulation.

Parameters	Values
Carrier frequency	5.405 GHz
Sampling frequency	46.9 MHz
Effective velocity	7100 m/s
Slant range	800,000 m
PRF	1663 Hz
Pulse width	51 μs
Pulse bandwidth	42.2 MHz
ISBR	60%
SIR	−30 dB
Pulse width of PRFI signal	10 μs, 15 μs, 20 μs, 25 μs

In the experiments, the sparse-term regularization parameter λ is generally set in a scale-normalized manner according to the dimensions of the data matrix. Since the low-rank and sparse decomposition in this study is performed in the Hankel-structured domain, for the Hankel matrix $\mathbf{R} \in \mathbb{C}^{L\times M}$ constructed from SAR pulses contaminated by PRFI, the regularization parameter λ can be set as

$$\lambda = \frac{1}{\sqrt{\mathbf{max}(L, M)}} \tag{41}$$

This parameter mainly controls the trade-off between the low-rank PRFI component and the sparse useful SAR signal component. Regarding the truncation rank parameter r in TNN, the TNN is defined as

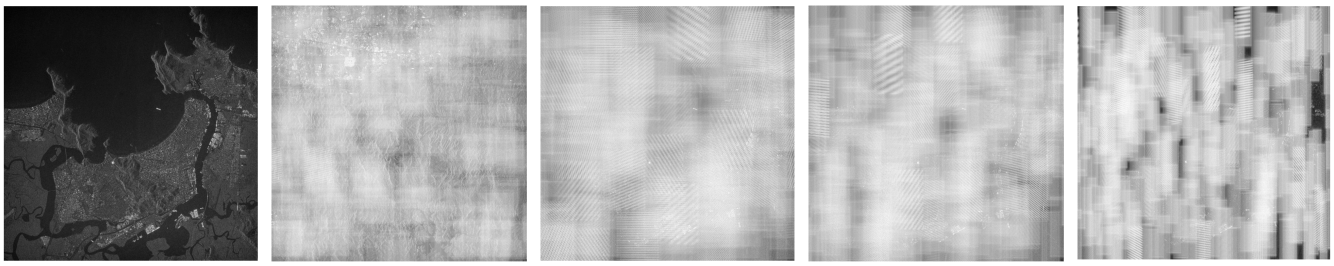
$$\|\mathbf{I}\|_{r,*} = \sum_{i=r+1}^{\min(m,n)} \sigma_i(\mathbf{I}) = \sum_{i=1}^{\min(m,n)} \sigma_i(\mathbf{I}) - \sum_{i=1}^{r} \sigma_i(\mathbf{I}) \tag{42}$$

where the first r dominant singular values are not penalized, and only the singular values from the $r+1$ *th* onward are summed and constrained. Existing TNN studies generally determine r according to the dominant rank or singular value distribution of the low-rank component to be recovered. In practical experiments, a small empirical value, such as $r = 1$, is often adopted to preserve the most dominant low-rank structure. Regarding the initial penalty parameter μ_0, in this study, μ_0 is related to the spectral norm and infinity norm of the observation matrix to ensure that the ADMM iterations maintain a relatively stable numerical scale under different data amplitudes:

$$\mu_0 = \frac{1.5}{\max\left(\| \mathbf{R} \|_2, \frac{\|\mathbf{R}\|_\infty}{\lambda}\right)} \tag{43}$$

Figure 5 presents the imaging results. Figure 5a shows the interference-free SAR image, while Figure 5b–e correspond to PRFI pulse widths of 10, 15, 20, and 25 μs, respectively. With the other interference parameters unchanged, increasing the PRFI pulse width extends its temporal occupancy and increases the number of contaminated range samples. Because the PRFI chirp rate is mismatched with the SAR matched filter, the interference cannot be correctly focused after pulse compression and appears as fog-like or stripe-like artifacts. From Figure 5b to Figure 5e, these artifacts become progressively more pronounced and

spatially extensive, resulting in reduced image contrast and increasingly obscured ground-feature details.



(**a**) (**b**) (**c**) (**d**) (**e**)

Figure 5. Imaging results of simulated PRFI for different pulse widths. (**a**) PRFI-free SAR image. (**b**–**e**) PRFI-contaminated SAR images with pulse widths of 10, 15, 20, and 25 μs, respectively. The ISBR is 60% and the SIR is **−30 dB**.

The results of simulated PRFI using FNF, TNF, RPCA, GBSLRSD and our approach are shown in Figure 6. The FNF's mitigating outcomes are illustrated in Figure 6a–d. The findings indicate that although the FNF approach can alleviate PRFI, the large bandwidth of PRFI causes significant spectral gaps, resulting in defocused SAR images. Additionally, it can be observed that the FNF method is not sensitive to changes in PRFI pulse width; when the PRFI bandwidth remains unchanged, the mitigation results do not deteriorate significantly with an increase in PRFI pulse width. The outcomes generated by the TNF approach are illustrated in Figure 6e–h. TNF can effectively alleviate PRFI. However, as the PRFI pulse width gradually increases, the mitigation performance of TNF decreases, leading to a reduction in SNR of the mitigated image. This issue is caused by the loss of useful signals due to pulse gaps after mitigation. Figure 6i–l show the results of the RPCA. It can be seen from the figures that it is not suitable for mitigating wideband PRFI. It not only leaves some PRFI artifacts but also loses a large number of valuable signals, deteriorating scene details. This is because the RPCA method relies on the traditional NN, which minimizes all singular values of the matrix simultaneously, leading to excessive penalization of singular values. This means that low-rank estimation is prone to errors, resulting in the loss of the signal's main components and introducing azimuth ambiguity. The PRFI mitigation results obtained using the GBSLRSD are shown in Figure 6m–p. It can be observed that the PRFI components are effectively removed, with no residual PRFI artifacts visible even in weak-echo regions. However, the excessive penalization of singular values imposed by the conventional NN causes over-decomposition of the sparse matrix representing the SAR signal component, thereby resulting in defocusing of the reconstructed SAR image. The experimental results of our approach are presented in Figure 6q–t. Our approach demonstrates a more effective mitigation of wideband PRFI. Compared to FNF, GBSLRSD and RPCA, the proposed method does not leave interference residues or cause the target to defocus due to the loss of valuable signals after mitigating wideband PRFI. Compared to TNF, the proposed method does not experience a decrease in mitigation performance due to an increase in PRFI content in the SAR data.

To better demonstrate the mitigation effects of our approach compared to the others, the regions of interest (ROI) in Figure 6 are enlarged and displayed in Figure 7. The ROIs were selected to highlight regions that can clearly present the details of the SAR images after interference mitigation, such as harbor ships, airport runways, and areas covered by interference artifacts. Interference mitigation outcomes of FNF and TNF are illustrated in Figure 7a,b, respectively. Due to the large bandwidth and long pulse width characteristics of this PRFI, the picture processed by FNF is significantly defocused, and the image processed by the TNF approach exhibits diminished SNR, losing intricate details. The outcome

processed by RPCA is illustrated in Figure 7c. It can be observed that RPCA exhibits a bias in low-rank component estimation, which not only causes residual interference artifacts but also results in the loss of valuable signals, leading to abnormal azimuth sidelobes for strong point targets. The magnified result obtained using GBSLRSD is shown in Figure 7d. Although no residual PRFI artifacts remain after GBSLRSD processing, the over-decomposition of the sparse matrix caused by the NN results in severe defocusing of the reconstructed SAR image. In contrast, the proposed method effectively removes interference components while preserving useful signals, even when dealing with PRFI of large bandwidth and long pulse width, allowing the mitigated SAR image to retain more ground feature details.

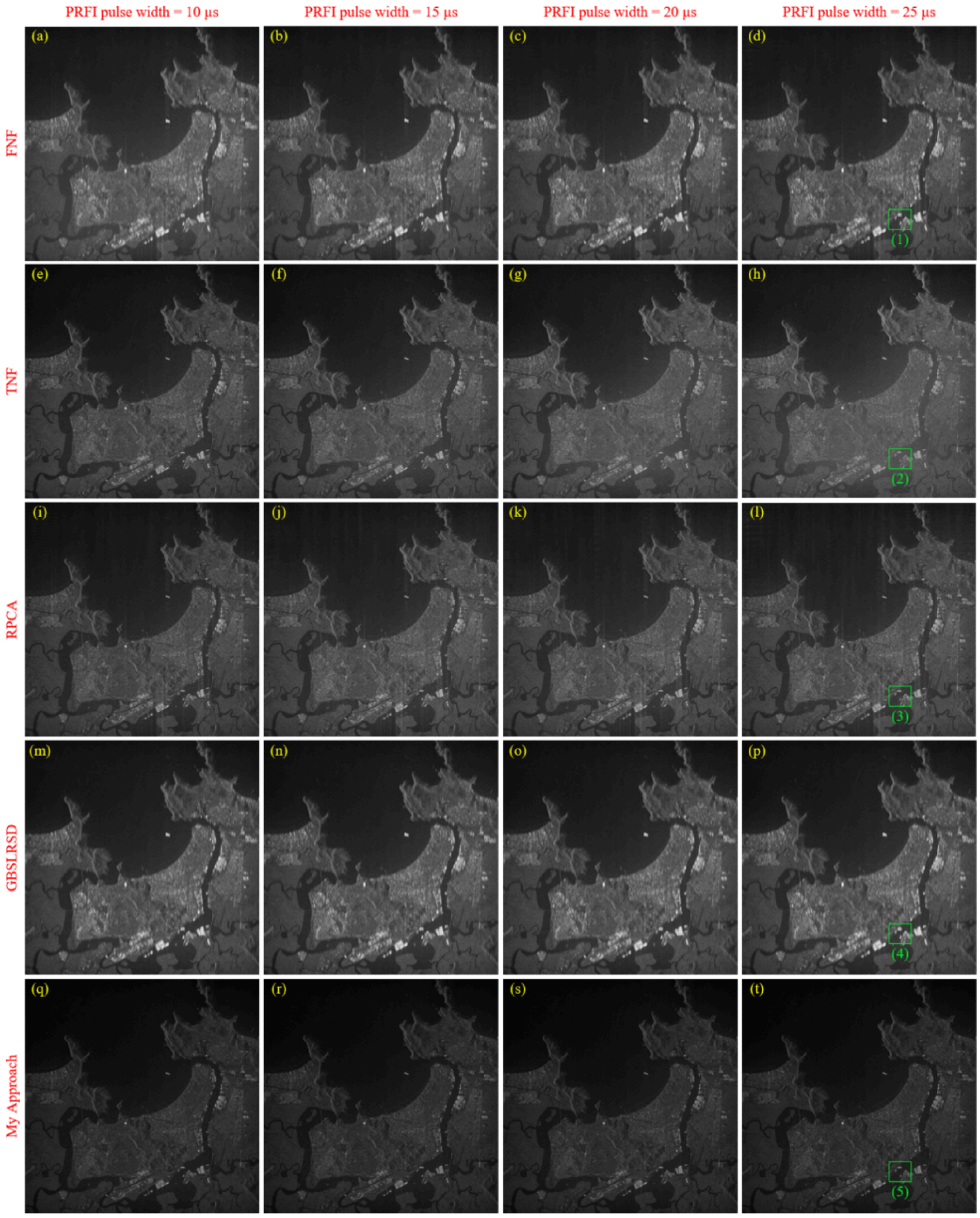


Figure 6. Mitigation results of simulated PRFI for different pulse widths and different methods. (**a**–**d**) Mitigation results of the FNF. (**e**–**h**) Mitigation results of the TNF. (**i**–**l**) Mitigation results of the RPCA. (**m**–**p**) Mitigation results of the GBSLRSD. (**q**–**t**) Mitigation results of the proposed method. (1)–(5) ROIs in (**d**), (**h**), (**l**), (**p**) and (**t**) with green boxes.

To further discuss the effectiveness of the method, RMSE is used as a quantitative analysis metric, with the analysis outcomes presented in Table 2. It can be observed from the table that our approach has the smallest RMSE, indicating that the processed data has minimal difference from the original data. When the PRFI pulse width is 10 μs, the mitigation effect of our approach is significantly better than others. As the PRFI pulse width increases, the RMSE of all methods rises. However, the TNF method's RMSE deteriorates the most severely, indicating that it is very sensitive to changes in interference pulse width. In contrast, the proposed method exhibits more robust mitigation performance and the best mitigation effect when facing variations in PRFI pulse width. This illustrates that our approach outperforms the other methods of comparison in terms of mitigation.



(**a**) (**b**) (**c**) (**d**) (**e**)

Figure 7. ROIs in Figure 6 with green boxes. (**a**–**e**) ROIs in Figure 6(1)–(5), respectively.

Table 2. RMSES of simulation experiment.

Method	PRFI PULSE WIDTH			
	10 μs	**15 μs**	**20 μs**	**25 μs**
FNF	0.3814	0.3841	0.4090	0.4653
TNF	0.1761	0.2955	0.4196	0.5345
RPCA	0.3657	0.3764	0.3873	0.4061
GBSLRSD	0.3599	0.3663	0.3946	0.4550
Proposed approach	**0.1028**	**0.1259**	**0.1392**	**0.1524**

4.3. Measured Experiment Results

(1) *Data Introduction:* The two PRFI-contaminated datasets used in the measured experiments are from the inland and coastal scenes of ESA Sentinel-1A. The introduction of the datasets is shown in Figure 8.

The first example observed area is located in the coastal region of Copenhagen, Denmark. The data's working mode is Sentinel-1A's interferometric wide (IW) swath, and the data used in the experiment is the 9th burst. The geographical location and ID are shown in Figure 8a. The amplitude image of the original echo data is presented in Figure 8c, where dense PRFI can be observed. Figure 8d is the azimuth-time range-frequency domain image, indicating that the PRFI bandwidth occupies more than half of the SAR bandwidth. Figure 8e illustrates the imaging outcome, wherein artifacts obscure the urban and port regions.

The second case is located in Bozhou, China, with its geographical information and data ID shown in Figure 8b. The amplitude image of this data is illustrated in Figure 8f. The PRFI is widely distributed across the echoes in this data. Figure 8g is the range spectrum, where the frequency components of strong PRFI change regularly with frequency. The imaging outcome appears in Figure 8h, where significant artifacts from strong PRFI cover the observed scene, severely affecting the interpretation and subsequent applications.

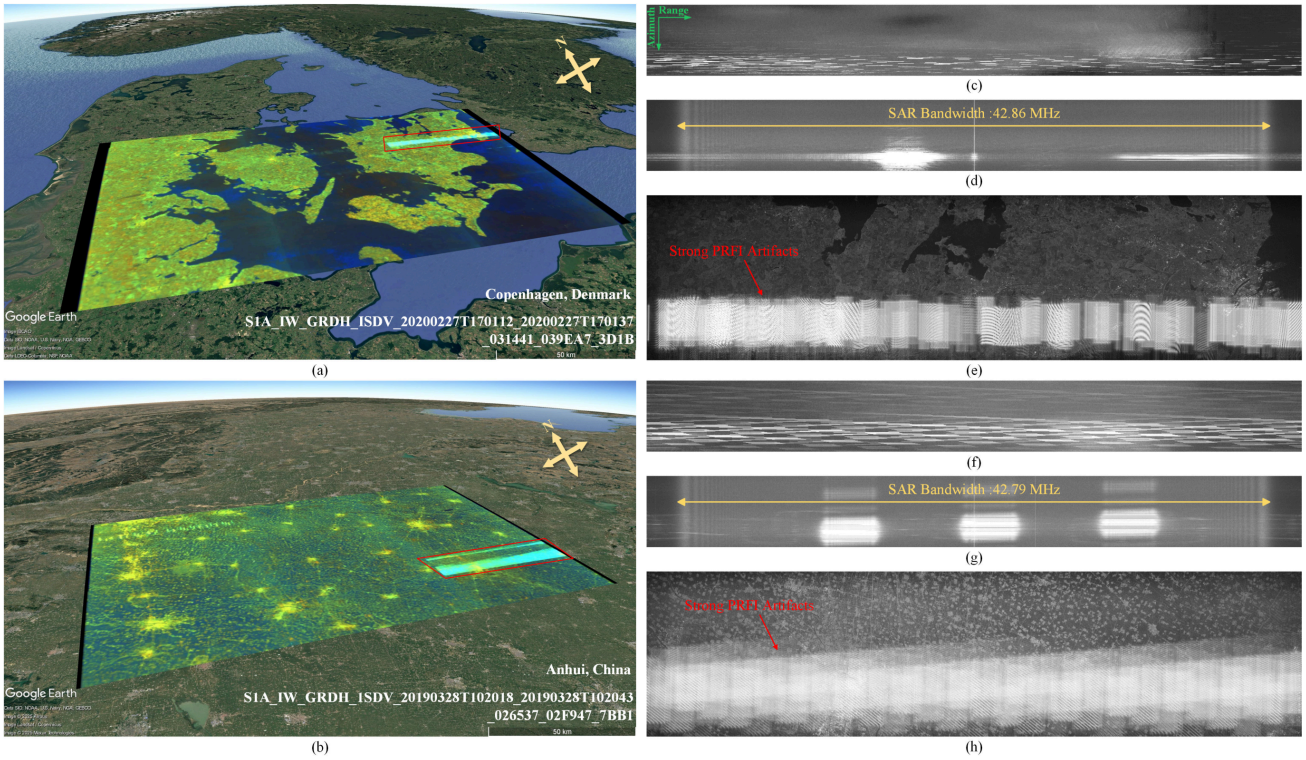


Figure 8. Description of measured data information: (**a**,**b**) geographic information; (**c**,**f**) SAR echoes; (**d**,**g**) the range spectrum of SAR echoes; (**e**,**h**) SAR images after imaging.

(2) *The experimental results of the first example:* Figure 9 presents the PRFI mitigation results. It can be seen from the figure that all approaches can mitigate strong PRFI artifacts to varying degrees. However, the quality of scene information recovery differs. The processing result of FNF is shown in Figure 9a. Since the PRFI bandwidth in this case almost spans the entire spectrum, the FNF method removes too many useful SAR signals while filtering out PRFI components. As seen from Figure 8b, PRFIs in the echo are dense, so the TNF method also loses some useful signals in Figure 9b. Therefore, as indicated by the red and blue circles marking the ROIs in Figure 9a,b, the scene after interference mitigation is blurred, and the SNR is severely reduced. Figure 9c shows RPCA's mitigation results. Compared to the first two methods, the RPCA method restores more details of ground objects in the red circle, but there is still PRFI residue in the blue circle. This is because the PRFI bandwidth is large, making it difficult for RPCA to distinguish the singular values, thus reducing the extraction accuracy of interference components. The interference mitigation result obtained using GBSLRSD is shown in Figure 9d. It can be observed that the PRFI artifacts are effectively removed; however, the ground-object information highlighted by the red circle is no longer clearly discernible. Figure 9e shows the proposed method's results. In this figure, the detailed information of the scene in the red circle is clear, and no PRFI artifacts remain in the sea area. To further demonstrate the detailed information of the experimental results, the ROIs marked by the yellow box are enlarged as shown in Figure 9(1)–(5). From Figure 9(1) and (2), it can be seen that the FNF and TNF methods lost too much useful signal, making the airport runway in the image blurry. Figure 9(3) shows residual PRFI artifacts. As shown in Figure 9(4), no residual PRFI artifacts are observed; however, the airport runway is no longer discernible. In Figure 9(5), PRFI artifacts are completely mitigated, and the airport runway is clearly visible, further illustrating the success of our approach.

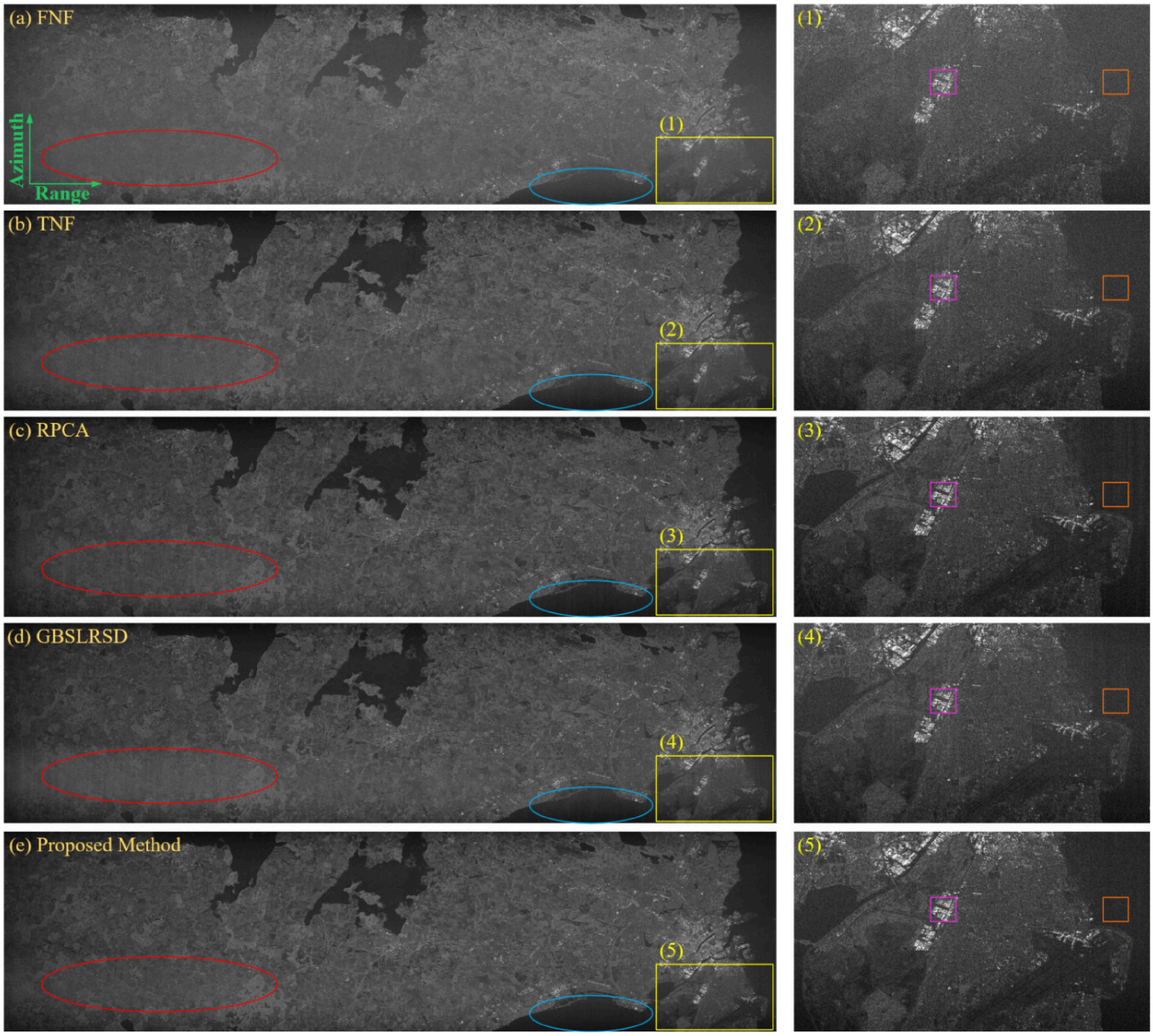


Figure 9. The experimental results of the first example. (**a**–**e**) The mitigation outcomes. (1)–(5) The ROIs marked by the yellow box.

(3) *The experimental results of the second example:* Figure 10 presents outcomes of this case. Figure 10a displays the result of FNF. Due to the presence of three wideband interference components that almost fill the azimuth time in the SAR spectrum, FNF causes numerous spectral gaps, leading to poor image SNR and a loss of detailed information. In the red circle, the information about the river and town in the SAR image has been eliminated. Figure 10b shows that the TNF method can effectively mitigate PRFI artifacts in land scenes; however, it also causes the loss of city detail information in the interference-covered area, as indicated by the red circle. The RPCA method's processing results are shown in Figure 10c. Due to the limitations of long pulse width and wide bandwidth, the RPCA method cannot mitigate all PRFI, leaving obvious interference artifacts that obscure two important target areas in the picture. As can be seen from Figure 10d, GBSLRSD mitigates most of the PRFI ghosting artifacts; however, some stripe-like PRFI signatures remain in the image. These weak residual PRFI signatures significantly hinder the interpretation of ground-object information in land scenes. The outcome of our approach is illustrated in Figure 10e. Compared to other methods, our approach not only completely eliminates PRFI but also preserves the image's detailed information. For a better qualitative analysis of the results,

the ROIs marked by the yellow boxes in the image are enlarged and displayed in Figure 10(1)–(5). As mentioned above, the FNF method causes the loss of ground object information in Figure 10(1), severely affecting subsequent image applications. Figure 10(3) shows PRFI artifacts left by the RPCA method covering the town and river. Weak residual PRFI signatures left by GBSLRSD can be clearly observed in the ROI of Figure 10(4). Compared to Figure 10(5), although the interference in Figure 10(2) is mitigated, the SNR is low, and the noise level in the image is high. From a qualitative analysis perspective, the image quality processed by our approach is significantly better than others.

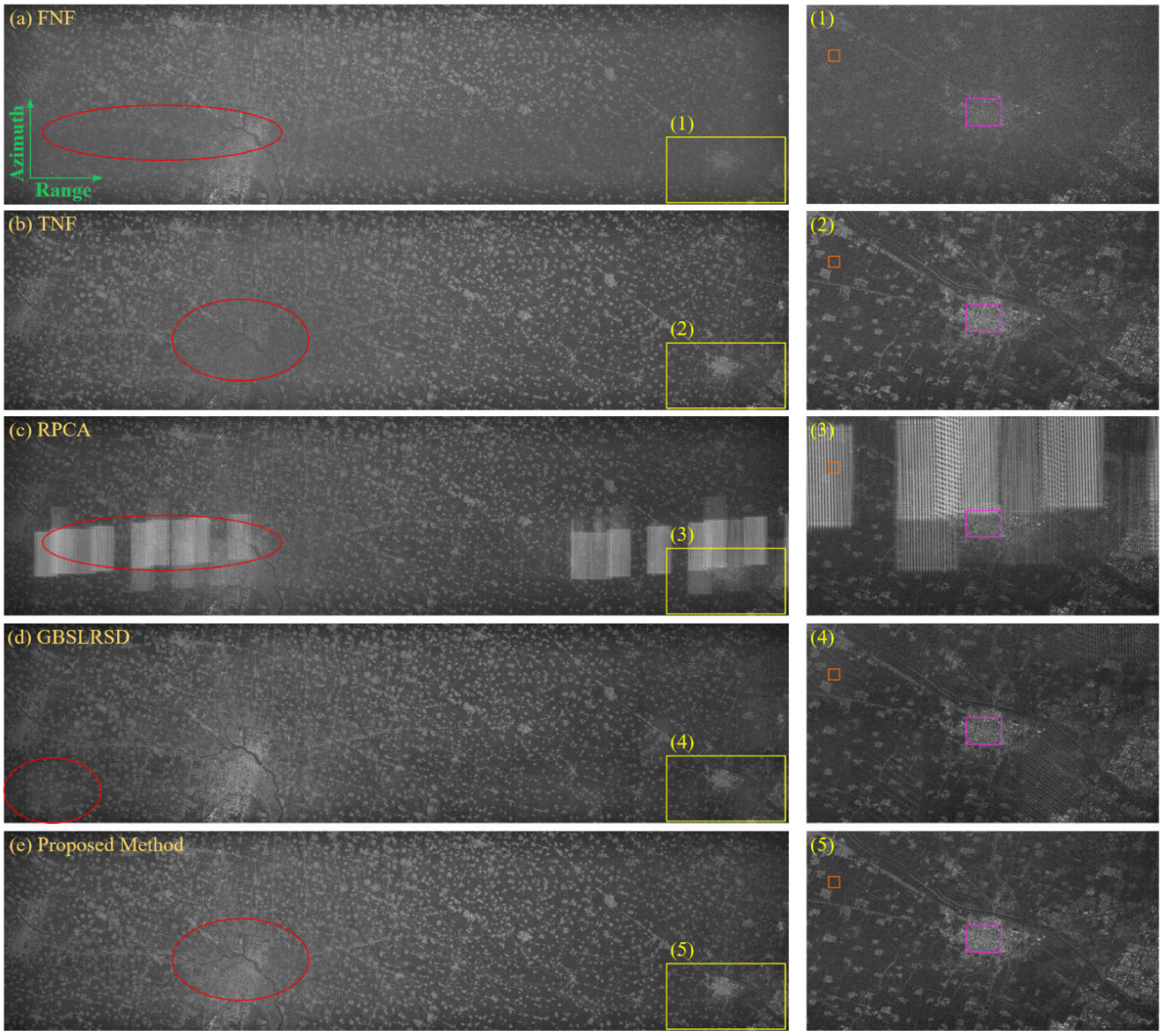


Figure 10. The experimental results of the second case. (**a**–**e**) The mitigation outcomes. (1)–(5) The ROIs marked by the yellow box in (**a**–**d**).

Further quantitative analysis indicators of our approach and the comparison approaches were calculated, with results presented in Table 3. The weak-echo region and the strong-echo region used for MNR are marked by the orange box and the purple box in Figures 9 and 10, respectively. Our approach has the smallest MNR, indicating that it has the best PRFI mitigation performance. The AG of our approach is higher than others, suggesting that the processed images contain richer detail information and have higher

quality restoration. Overall, these two quantitative analysis indicators further validate the effectiveness and advantages of our approach.

Table 3. The quantitative analysis of the measured experiment.

Method	Example 1		Example 2	
	MNR (dB)	AG	MNR (dB)	AG
FNF	−10.423	1.311	−2.537	1.288
TNF	−14.130	2.192	−6.784	2.583
RPCA	−15.231	3.762	0.806	3.840
GBSLRSD	−15.656	2.339	−5.098	3.697
Proposed approach	**−18.720**	**4.365**	**−8.048**	**4.557**

4.4. Runtime Analysis

To quantitatively evaluate the computational efficiency of the compared methods, the running times of FNF, TNF, RPCA, GBSLRSD, and the proposed method were measured under identical hardware and software conditions. To reduce the influence of random variations, each method was executed 10 times. The reported running times exclude non-algorithmic operations, such as data loading, disk writing, and result visualization.

The average running times of different methods are compared in Table 4. It can be observed that FNF and TNF achieve the lowest computational cost due to their simple processing structures, while RPCA requires the longest running time owing to the repeated SVD operations. The proposed approach reduces the computational time by approximately **35%** compared with RPCA. Although the proposed approach involves an iterative optimization procedure, it achieves a reasonable computational efficiency while providing superior RFI suppression performance.

Table 4. Quantitative comparison of average running time in measured experiments.

Method	Example 1	Example 2
	The Average Runtime (s)	The Average Runtime (s)
FNF	1.2714	1.0447
TNF	1.4649	1.3632
RPCA	1359.1193	1149.4944
GBSLRSD	255.0385	192.8531
Proposed approach	**873.0276**	**748.7537**

5. Discussion

The experimental results on both simulated and measured datasets verify the two pillars of the proposed method. First, as shown in Figure 3c, the Hankel-structured pulse exhibits fewer dominant singular values—that is, a lower rank—together with a steeper singular-value decay, which demonstrates that the Hankel structure constructed through TDE can enhance the low-rank property of PRFI. In addition, the TNN regularization adopted in the proposed method avoids the over-penalization of singular values inherent in conventional NN. This conclusion is corroborated by a comparison with RPCA and GBSLRSD, which rely on the same low-rank prior but use conventional NN. In the quantitative analysis of the simulation experiments in Table 2, the RMSE of the proposed method remains stable between 0.1028 and 0.1524 as the PRFI pulse width varies from 10 to 25 μs, whereas the RMSE of RPCA deteriorates to between 0.3657 and 0.4061. Compared with RPCA, the proposed method reduces the RMSE by **62.47–71.89%**, indicating a markedly improved recovery accuracy of the PRFI component. In the Bozhou measured data, RPCA

leaves visible stripe-like residual interference that obscures the river and town areas in Figure 10c, whereas the proposed Hankel + TNN regularized model recovers these features cleanly, as shown in Figure 10e. In the quantitative analysis of the two measured experiments, the AG is improved by **16.03%** and **18.67%** and the MNR is reduced by **3.06 dB** and **1.26 dB**, respectively, over the best competing method, quantitatively confirming the superior mitigation performance of the proposed Hankel + TNN regularized model in real-world PRFI scenarios.

Beyond the comparison with the low-rank-prior-based method, the advantages of the proposed method over conventional notch-filtering methods [8,31] also merit discussion. The quantitative analysis in Table 2 further corroborates the limitations of such methods. When the PRFI bandwidth is large, FNF produces extensive spectral gaps and its RMSE deteriorates to between 0.3814 and 0.4653; relative to FNF, the proposed method reduces the RMSE by **65.18–73.05%**. As the PRFI pulse width increases, TNF removes excessive useful signal and its RMSE deteriorates sharply from 0.1761 to 0.5345. By contrast, the proposed method neither notches the frequency domain nor zeros out time-domain samples; instead, it performs low-rank decomposition in the Hankel domain in a non-destructive manner, thereby circumventing both types of limitations simultaneously.

Against the backdrop of an increasingly congested electromagnetic environment, a growing number of reports [41,44,45] indicate that wideband PRFI will become more and more frequent. Since the proposed framework makes no assumption on the PRFI modulation type and operates on Level-0 raw echoes, it is readily transferable across SAR systems and remains compatible with downstream imaging, interferometric, and polarimetric applications. Despite its favorable wideband PRFI mitigation performance on both simulated and measured data, the proposed method has several limitations. It relies on the low-rank property of the Hankel-structured PRFI and the low-rank–sparse separability between the PRFI and useful SAR signal components. Its performance may therefore degrade when the interference is highly nonstationary, multiple interference sources overlap severely, or the interference component has a relatively high effective rank. In addition, the truncation parameter r, regularization parameter λ, and detection threshold ψ remain partly data-dependent. Pulse-by-pulse Hankel construction and iterative SVD operations also introduce considerable computational cost, limiting the current implementation in real-time processing. Several limitations point to future research directions: (1) since semi-parametric methods are computationally heavier than non-parametric ones, future work will further investigate wideband RFI and aim to develop lower-complexity algorithms; and (2) combining the proposed model-based approach with data-driven deep-learning components is expected to further broaden the applicability of the proposed framework.

6. Conclusions

PRFI from ground-based radar sensors typically features wide bandwidth, which reduces the effectiveness of previously common notch filtering methods and low-rank decomposition methods based on traditional NNs. To address this issue, this paper establishes mathematical and geometric models of PRFI. A method based on the low-rank approximation model using Hankel structure and TNN regularization is proposed. This method first linearly extends the low-rank properties of PRFI in SAR echoes through Hankel structure, then employs TNN regularization to constrain PRFI, and, finally, solves the optimization problem of the low-rank approximation model based on TNN regularization using a two-stage iterative algorithm. The proposed method not only addresses the problem of losing too much useful signal in notch filtering methods but also overcomes the

errors in low-rank approximation caused by the over-penalization of singular values in traditional NNs.

Simulation experiments were conducted using different PRFI parameters to verify and discuss the mitigation performance of our approach. These findings indicate that our approach exhibits greater mitigation performance for wide-bandwidth PRFI compared to traditional methods. Measured experiments based on ESA Sentinel-1A further validated the effectiveness of our approach.

Author Contributions: Conceptualization, B.C. and Z.L.; methodology, B.C.; validation, B.C. and S.C.; formal analysis, B.C.; investigation, B.C.; resources, B.C., W.F. and F.Z.; data curation, B.C.; writing—original draft preparation, B.C.; writing—review and editing, B.C., Z.L. and W.F.; visualization, B.C.; supervision, W.F. and F.Z.; funding acquisition, W.F. and F.Z. All authors have read and agreed to the published version of the manuscript.

Funding: This research was funded by the National Natural Science Foundation of China under Grant U2541202, 62001350, 62425113.

Data Availability Statement: The experimental data were acquired from the European Space Agency Copernicus Data Space Ecosystem (https://dataspace.copernicus.eu/).

Conflicts of Interest: The authors declare no conflicts of interest.

References

1. DeGraaf, S.R. SAR imaging via modern 2-D spectral estimation methods. *IEEE Trans. Image Process.* **1998**, *7*, 729–761. [CrossRef] [PubMed]
2. Pu, W. Deep SAR Imaging and Motion Compensation. *IEEE Trans. Image Process.* **2021**, *30*, 2232–2247. [CrossRef] [PubMed]
3. Jordan, R.L.; Huneycutt, B.L.; Werner, M. The SIR-C/X-SAR synthetic aperture radar system. *Proc. IEEE* **1991**, *79*, 827–838. [CrossRef]
4. Albaba, A.; Bauduin, M.; Sakhnini, A.; Sahli, H.; Bourdoux, A. Sidelobes and Ghost Targets Mitigation Technique for High-Resolution Forward-Looking MIMO-SAR. *IEEE Trans. Radar Syst.* **2024**, *2*, 237–250. [CrossRef]
5. Reinecke, M.; Noegel, T.; Sura, O.; Hoffmann, M.; Gulden, P.; Vossiek, M. Mitigation of Mirror Targets in Automotive Forward-Looking Synthetic Aperture Radar. *IEEE Trans. Radar Syst.* **2025**, *3*, 982–994. [CrossRef]
6. Tao, M.; Su, J.; Huang, Y.; Wang, L. Mitigation of Radio Frequency Interference in Synthetic Aperture Radar Data: Current Status and Future Trends. *Remote Sens.* **2019**, *11*, 2438. [CrossRef]
7. Misra, S.; de Matthaeis, P. Passive remote sensing and radio frequency interference (RFI): An overview of spectrum allocations and RFI management algorithms. *IEEE Geosci. Remote Sens. Mag.* **2014**, *2*, 68–73. [CrossRef]
8. Li, N.; Lv, Z.; Guo, Z.; Zhao, J. Time-Domain Notch Filtering Method for Pulse RFI Mitigation in Synthetic Aperture Radar. *IEEE Geosci. Remote Sens. Lett.* **2022**, *19*, 4013805. [CrossRef]
9. Li, N.; Lv, Z.; Guo, Z. Pulse RFI Mitigation in Synthetic Aperture Radar Data via a Three-Step Approach: Location, Notch, and Recovery. *IEEE Trans. Geosci. Remote Sens.* **2022**, *60*, 5225617. [CrossRef]
10. Huang, Y.; Zhao, B.; Tao, M.; Chen, Z.; Hong, W. Review of synthetic aperture radar interference suppression. *J. Radars* **2020**, *9*, 86–106. [CrossRef]
11. Lord, R.T.; Inggs, M.R. Efficient RFI suppression in SAR using LMS adaptive filter integrated with range/Doppler algorithm. *Electron. Lett.* **1999**, *35*, 629. [CrossRef]
12. Le, C.T.; Hensley, S.; Chapin, E. Adaptive filtering of RFI in wideband SAR signals. In Proceedings of the 7th Annual JPL AirSAR Workshop, Pasadena, CA, USA, 12–16 January 1998; pp. 41–50.
13. Bugallo, M.F.; Miguez, J.; Castedo, L. A maximum likelihood approach to blind multiuser interference cancellation. *IEEE Trans. Signal Process.* **2001**, *49*, 1228–1239. [CrossRef]
14. Liu, Z.; Liao, G.; Yang, Z. Time variant RFI suppression for SAR using iterative adaptive approach. *IEEE Geosci. Remote Sens. Lett.* **2013**, *10*, 1424–1428. [CrossRef]
15. Yang, Z.; Du, W.; Liu, Z.; Liao, G. WBI Suppression for SAR Using Iterative Adaptive Method. *IEEE J. Sel. Top. Appl. Earth Obs. Remote Sens.* **2017**, *9*, 1008–1014. [CrossRef]
16. Han, W.; Bai, X.; Fan, W.; Wang, L.; Zhou, F. Wideband interference suppression for SAR via instantaneous frequency estimation and regularized time-frequency filtering. *IEEE Trans. Geosci. Remote Sens.* **2022**, *60*, 5208612. [CrossRef]

17. Ruan, H.; Ye, W.; Yin, C.; Zhang, S. Wide band noise interference suppression for SAR with dechirping and eigensubspace filtering. In Proceedings of the 2010 International Conference on Intelligent Control and Information Processing, Dalian, China, 13–15 August 2010; pp. 39–42. [CrossRef]
18. Nie, G.; Liao, G.; Zeng, C.; He, X. Off-Grid RFI Suppression Method in Synthetic Aperture Radar Based on Mismatch Reconstruction and Dictionary Rotation. *IEEE J. Sel. Top. Appl. Earth Obs. Remote Sens.* **2023**, *16*, 3988–3999. [CrossRef]
19. Qiu, T.; Sun, X.; Zheng, H.; Wang, W.; Zhang, Y.; Liu, C. A Scheme for Extracting Weak RFI Parameters Based on TJLS Matrix Decomposition. *IEEE Geosci. Remote Sens. Lett.* **2024**, *21*, 4005605. [CrossRef]
20. Mao, Y.; Huang, Y.; Yu, X.; Chen, X.; Zhang, Z.; Chen, Z.; Hong, W. A Novel Group-Parametric Model for RFI Suppression on Spaceborne SAR. *IEEE Trans. Geosci. Remote Sens.* **2025**, *63*, 5201314. [CrossRef]
21. Zhang, L.; Luo, Y.; Wang, H.; Zhang, Q. Suppression of Mainlobe Interference in Radar Network via Joint Low-Rank and Sparse Recovery. *IEEE Trans. Radar Syst.* **2024**, *2*, 303–317. [CrossRef]
22. Nguyen, L.H.; Tran, T.; Do, T. Sparse models and sparse recovery for ultra-wideband SAR applications. *IEEE Trans. Aerosp. Electron. Syst.* **2014**, *50*, 940–958. [CrossRef]
23. Joy, S.; Nguyen, L.H.; Tran, T.D. Joint down-range and cross-range RFI suppression in ultra-wideband SAR. *IEEE Trans. Geosci. Remote Sens.* **2021**, *59*, 3136–3149. [CrossRef]
24. Su, J.; Tao, H.; Tao, M.; Wang, L.; Xie, J. Narrow-band interference suppression via RPCA-based signal separation in time–frequency domain. *IEEE J. Sel. Top. Appl. Earth Obs. Remote Sens.* **2017**, *10*, 5016–5025. [CrossRef]
25. Guan, X.; Huang, Y.; Chen, J.; Mao, Y.; Chen, X.; Chen, Z.; Chen, J.; Hong, W. An RFI Mitigation Method on Spaceborne SAR via Kurtosis-Based Reweighted Nuclear Norm. *IEEE Trans. Geosci. Remote Sens.* **2025**, *63*, 5216518. [CrossRef]
26. Yang, H.; Chen, C.; Chen, S.; Xi, F.; Liu, Z. A dictionary-based SAR RFI suppression method via robust PCA and chirp scaling algorithm. *IEEE Geosci. Remote Sens. Lett.* **2021**, *18*, 1229–1233. [CrossRef]
27. Huang, Y.; Zhang, L.; Li, J.; Chen, Z.; Yang, X. Reweighted tensor factorization method for SAR narrowband and wideband interference mitigation using smoothing multiview tensor model. *IEEE Trans. Geosci. Remote Sens.* **2020**, *58*, 3298–3313. [CrossRef]
28. Huang, Y.; Chen, Z.; Wen, C.; Li, J.; Xia, X.-G.; Hong, W. An efficient radio frequency interference mitigation algorithm in real synthetic aperture radar data. *IEEE Trans. Geosci. Remote Sens.* **2022**, *60*, 5224912. [CrossRef]
29. Lu, X.; Yang, J.; Yeo, T.S.; Su, W.; Gu, H.; Yu, W. Accurate SAR image recovery from RFI contaminated raw data by using image domain mixed regularizations. *IEEE Trans. Geosci. Remote Sens.* **2022**, *60*, 5102813. [CrossRef]
30. Su, J.; Xi, M.; Gong, Y.; Tao, M.; Fan, Y.; Wang, L. Time-varying wideband interference mitigation for SAR via time-frequency-pulse joint decomposition algorithm. *IEEE Trans. Geosci. Remote Sens.* **2022**, *60*, 5118816. [CrossRef]
31. Cazzaniga, G.; Guarnieri, A.M. Removing RF interferences from P-band airplane SAR data. In Proceedings of the 1996 International Geoscience and Remote Sensing Symposium, Lincoln, NE, USA, 31 May 1996; pp. 1845–1847. [CrossRef]
32. Zhou, F.; Wu, R.; Xing, M.; Bao, Z. Eigensubspace-based filtering with application in narrow-band interference suppression for SAR. *IEEE Geosci. Remote Sens. Lett.* **2007**, *4*, 75–79. [CrossRef]
33. Tao, M.; Zhou, F.; Liu, J.; Zhang, Z.; Bao, Z. Narrow-band interference mitigation for SAR using independent subspace analysis. *IEEE Trans. Geosci. Remote Sens.* **2014**, *52*, 5289–5301. [CrossRef]
34. Zhou, F.; Xing, M.; Bai, X.; Sun, G.; Bao, Z. Narrow-band interference suppression for SAR based on complex empirical mode decomposition. *IEEE Geosci. Remote Sens. Lett.* **2009**, *6*, 423–427. [CrossRef]
35. Zhou, F.; Tao, M.; Bai, X.; Liu, J. Narrow-band interference suppression for SAR based on independent component analysis. *IEEE Trans. Geosci. Remote Sens.* **2013**, *51*, 4952–4960. [CrossRef]
36. Chen, B.; Lv, Z.; Lu, P.; Shu, G.; Huang, Y.; Li, N. Extension and Evaluation of SSC for Removing Wideband RFI in SLC SAR Images. *Remote Sens.* **2022**, *14*, 4294. [CrossRef]
37. Huang, Y.; Wen, C.; Chen, Z.; Chen, J.; Liu, Y.; Li, J.; Hong, W. HRWS SAR narrowband interference mitigation using low-rank recovery and image-domain sparse regularization. *IEEE Trans. Geosci. Remote Sens.* **2022**, *60*, 5217914. [CrossRef]
38. Yang, H.; Lang, P.; He, Y.; Lu, X.; Liu, Z.; Yang, J. Lambda-1 Detector: Adaptive Interference Detection in Synthetic Aperture Radar Images. *IEEE Trans. Geosci. Remote Sens.* **2025**, *63*, 5202613. [CrossRef]
39. Yang, H.; Li, K.; Li, J.; Du, Y.; Yang, J. BSF: Block Subspace Filter for Removing Narrowband and Wideband Radio Interference Artifacts in Single-Look Complex SAR Images. *IEEE Trans. Geosci. Remote Sens.* **2022**, *60*, 5211916. [CrossRef]
40. Yang, H.; Lang, P.; Lu, X.; Chen, S.; Xi, F.; Liu, Z.; Yang, J. Robust Block Subspace Filtering for Efficient Removal of Radio Interference in Synthetic Aperture Radar Images. *IEEE Trans. Geosci. Remote Sens.* **2024**, *62*, 5206812. [CrossRef]
41. Chen, J.; Tao, M.; Liu, Y.; Li, T.; Liu, Y.; Li, J.; Tang, C.; Li, J.; Wang, L. Characterization and Mitigation of Radio Frequency Interference Signatures in L-Band LuTan-1 InSAR System: First Results and Assessment. *IEEE Trans. Radar Syst.* **2024**, *2*, 404–420. [CrossRef]
42. Lv, Z.; Fan, H.; Chen, Z.; Qiu, J.; Ren, M.; Zhang, Z. Mitigate the LFM-PRFI in SAR Data: Joint Down-Range and Cross-Range Filtering. *IEEE Trans. Geosci. Remote Sens.* **2023**, *61*, 5205918. [CrossRef]

43. Zhou, T.; Tao, D. GoDec: Randomized low-rank & sparse matrix decomposition in noisy case. In Proceedings of the 28th International Conference on Machine Learning, Bellevue, WA, USA, 28 June–2 July 2011; pp. 33–40.
44. Li, N.; Lv, Z.; Guo, Z. Observation and Mitigation of Mutual RFI Between SAR Satellites: A Case Study Between Chinese GaoFen-3 and European Sentinel-1A. *IEEE Trans. Geosci. Remote Sens.* **2022**, *60*, 5112819. [CrossRef]
45. Li, N.; Hu, X. Ultrawideband Mutual RFI Mitigation Between SAR Satellites: From the Perspective of European Sentinel-1A. *IEEE Trans. Geosci. Remote Sens.* **2024**, *62*, 5229020. [CrossRef]
46. Ding, Y.; Fan, W.; Tao, M.; Zhang, Z.; Wang, L.; Zhou, F.; Lu, B. Wideband interference mitigation for synthetic aperture radar based on the variational Bayesian method. *Signal Process.* **2022**, *198*, 108581. [CrossRef]
47. Hu, Y.; Zhang, D.; Ye, J.; Li, X.; He, X. Fast and Accurate Matrix Completion via Truncated Nuclear Norm Regularization. *IEEE Trans. Pattern Anal. Mach. Intell.* **2013**, *35*, 2117–2130. [CrossRef] [PubMed]
48. Cai, J.F.; Candès, E.J.; Shen, Z. A Singular Value Thresholding Algorithm for Matrix Completion. *SIAM J. Optim.* **2010**, *20*, 1956–1982. [CrossRef]
49. Zhang, Y.-S.; Li, Z.-Y.; Pang, D.-D.; Wang, L.-Y.; Wu, C.-J.; Duan, K.; Gao, J.-M. Fast Low Rank and Sparse Decomposition Based on Greedy Bilateral Smoothing for Infrared Small Target Detection. *IEEE Access* **2024**, *12*, 196740–196755. [CrossRef]

Disclaimer/Publisher's Note: The statements, opinions and data contained in all publications are solely those of the individual author(s) and contributor(s) and not of MDPI and/or the editor(s). MDPI and/or the editor(s) disclaim responsibility for any injury to people or property resulting from any ideas, methods, instructions or products referred to in the content.